Mesoporous MoS$_2$ as a Transition Metal Dichalcogenide Exhibiting Pseudocapacitive Li and Na-Ion Charge Storage

John B. Cook, Hyung-Seok Kim, Yan Yan, Jesse S. Ko, Shauna Robbennolt, Bruce Dunn,* and Sarah H. Tolbert*

The ion insertion properties of MoS$_2$ continue to be of widespread interest for energy storage. While much of the current work on MoS$_2$ has been focused on the high capacity four-electron reduction reaction, this process is prone to poor reversibility. Traditional ion intercalation reactions are highlighted and it is demonstrated that ordered mesoporous thin films of MoS$_2$ can be utilized as a pseudocapacitive energy storage material with a specific capacity of 173 mAh g^{-1} for Li-ions and 118 mAh g^{-1} for Na-ions at 1 mV s^{-1}. Utilizing synchrotron grazing incidence X-ray diffraction techniques, fast electrochemical kinetics are correlated with the ordered porous structure and with an iso-oriented crystal structure. When Li-ions are utilized, the material can be charged and discharged in 20 seconds while still achieving a specific capacity of 140 mAh g^{-1}. Moreover, the nanoscale architecture of mesoporous MoS$_2$ retains this level of lithium capacity for 10 000 cycles. A detailed electrochemical kinetic analysis indicates that energy storage for both ions in MoS$_2$ is due to a pseudocapacitive mechanism.

1. Introduction

Pseudocapacitive charge storage is emerging as an exciting means of storing energy which could find applications ranging from electric vehicles to fast charging portable electronics. This type of charge storage may alleviate the fundamental kinetic barriers associated with solid-state diffusion processes that lead to long charging times in traditional batteries. The power density in Li-ion batteries is fundamentally limited because faradaic (i.e., charge transfer) reactions in those electrode materials involve solid-state ionic diffusion (10^{-10}–10^{-15} cm^2 s^{-1}), which leads to slow charging and discharging times.[1,2] In contrast, electric

double layer capacitors (EDLCs) exhibit high power density by storing charge on a high surface area material (usually carbon).[3–5] However, the total available capacity of the active material is limited by electrostatic repulsion,[6] leading to specific capacitances of only ≈100 F g^{-1}.[3,7] Pseudocapacitance is another type of charge storage mechanism that combines the dynamic response of EDLCs with the high energy density of batteries through faradaic reactions that display capacitor-like kinetics.[8–10] Pseudocapacitance occurs by charge transfer at or near the surface of a redox active material, and can offer specific capacitances greater than 1000 F g^{-1}.[11–14] Realization and application of these materials represent the next frontier in the development of fast energy storage technology.

Pseudocapacitive charge storage has been described as being either an intrinsic property or an extrinsic property of a material. Intrinsic pseudocapacitive materials,[12] such as RuO$_2$·xH$_2$O,[15] MnO$_2$,[16] and Nb$_2$O$_5$,[17,18] display pseudocapacitance for a wide range of particle sizes and morphologies. The electrochemical properties of an extrinsic pseudocapacitor material, on the other hand, depend on the particle size. Unfortunately, intrinsic pseudocapacitor materials are not abundant and this has led our group to focus on the development of various extrinsic materials. For example, in a recent publication, we have carefully examined MoO$_2$, which is an extrinsic pseudocapacitor material that does not exhibit pseudocapacitance in bulk form.[19] Synthesis of the material with a hierarchical nanoscale architecture, however, led to charge storage through a pseudocapacitive mechanism. The key finding was that pseudocapacitance arises in an extrinsic material when three key criteria are met: 1) No phase changes occur upon ion insertion and deinsertion, 2) ion diffusion path lengths are reduced by nanostructuring the material, and 3) there is good electronic conductivity within the active material, between particles, and to the current collector. Certain distinct electrochemical features characterize pseudocapacitive charge storage processes. For example, in cyclic voltammetry (CV), redox peaks show a small voltage offset between oxidation/reduction peaks, which is indicative of reversible reactions and fast charge transfer processes.[12]

Pseudocapacitance has been demonstrated in many transition metal oxide-based materials,[20–23] but transition metal sulfides, while studied, and even commercialized as battery

J. B. Cook, Y. Yan, S. Robbennolt, S. H. Tolbert
Department of Chemistry and Biochemistry
UCLA
Los Angeles, CA 90095-1569, USA
E-mail: tolbert@chem.ucla.edu
H.-S. Kim, J. S. Ko, B. Dunn, S. H. Tolbert
Department of Materials Science and Engineering
UCLA
Los Angeles, CA 90095-1595, USA
E-mail: bdunn@ucla.edu
B. Dunn, S. H. Tolbert
The California NanoSystems Institute
UCLA
Los Angeles, CA 90095, USA

ADVANCED
ENERGY
MATERIALS
www.advenergymat.de

Materials
Views
www.MaterialsViews.com

materials, are a mostly unexplored area for capacitive charge storage.[24,25] Metal chalcogenides are promising pseudocapacitive candidates because of their anisotropic crystal structures, which have large interlayer atomic spacings that can allow for facile ion diffusion. The thermodynamically stable phase of MoS_2 is the 2H form, consisting of trigonal prismatic coordination of sulfur around the molybdenum and weak van der Waals stacking along the c-axis of the unit cell.[26] The van der Waals gaps are 6.2 Å in large crystals and can be expanded to 6.9 Å in nanostructured samples.[27,28] The large van der Waals gaps should be ideal for fast 2D Li-ion diffusion, but they have not been well exploited as most studies have focused on high capacity, four electron reduction reactions that destroy these diffusion pathways as discussed below.

MoS_2 has been well studied as a high capacity electrode material, achieving up to 1290 mAh g^{-1} when cycled with Li-ions to 0 V versus Li/Li^{+}[29,30] and 854 mAh g^{-1} when cycled with Na-ions to 0 V versus Na/Na^{+}.[31] In situ X-ray diffraction combined with Fourier Transform Infrared Spectroscopy (FTIR) spectroscopy has revealed that when MoS_2 is cycled to these very low potentials to achieve these very high capacities, molybdenum metal nanoparticles are formed within a Li_2S matrix, and subsequent electrochemical cycling operates as a lithium–sulfur redox couple.[32] In the analogous experiment of cycling MoS_2 to 0 V versus Na/Na^{+}, X-ray diffraction confirmed the formation of Na_2S, demonstrating that this, too, is a conversion-type reaction.[33] While high capacities are achieved at these low potentials with both Li-ions and Na-ions, the parent crystalline atomic structure is completely destroyed and does not reform after the Li or Na is removed.[32,33] Furthermore, these diffusive phase changes are kinetically hindered, thereby precluding pseudocapacitive behavior, which relies on rapid kinetics.

In the 1980s, MoS_2 was seriously considered as an intercalation-host cathode for a commercial Li-ion battery. In the original 1980 Moli Energy LTD patent, it was reported that MoS_2 exhibited long lifetimes when cycled in a limited voltage region.[34,35] Early structural characterization of this insertion reaction, and more recent work that includes the sodium insertion reaction, shows that limiting the cycling voltage between 1.0–3.0 V versus Li/Li^{+} or 0.5–2.6 V versus Na/Na^{+} corresponds to the insertion of ≈1 mole of Li or Na in Li_xMoS_2 or Na_xMoS_2, without destroying the 2D atomic layered structure.[36–38] The work presented in the Moli Energy LTD patent and subsequent peer reviewed works on MoS_2 as an intercalation host highlighted the high energy density (with a Li anode) and good cycling lifetime.[34,35] However, bulk MoS_2 powders produce a battery material that requires charging times between 3 and 10 hours to realize the highest capacities and longest cycle lifetimes.[34,39] Nanostructuring MoS_2 represents a method to cross over from this slow battery-type charge storage, to a fast pseudocapacitive charge storage mechanism.

A number of methods have been developed to synthesize nanostructured MoS_2. For example, multiple hydrothermal syntheses have been utilized to produce various nanostructured forms of MoS_2.[40–42] These syntheses tended to produce fairly disordered crystal structures and do not lead to homogeneous microstructures. In order to better control the morphology of MoS_2 nanomaterials, Yu et al. synthesized 5 nm dispersible MoS_2 nanoparticles from $Mo(CO)_6$ and sulfur using a

coordinating solvent.[43] The low temperatures utilized in that work, however, led to nanoparticles with low crystallinity and poor lamellar stacking along the c-axis direction. Another synthesis technique demonstrated by Lou and Zeng utilizes a two-step process in which hydrothermally synthesized α-MoO_3 nanowires are converted to MoS_2 by thermal sulfurization in H_2S.[44] The original oxide morphology was retained after the sulfurization process, and the particles exhibited good crystallinity presumably because of the high conversion temperature (10 h at 600 °C). More extensive discussion of the various methods used to synthesize MoS_2 has been reviewed.[29,45–47]

Even though nanoparticle-based materials are advantageous for their short ion-diffusion path lengths, they do not usually form ideal electrode architectures with carbon and binders. Inhomogeneous nanoparticle agglomerates tend to form, which are difficult to disperse in a conductive additive and result in resistive interparticle electrical contact, leading to poor electronic conduction.[48] In order to address these issues, we utilize mesoporous nanostructures that make use of three important qualities that give rise to pseudocapacitive behavior: (1) The ion diffusion path lengths are limited to within the nanoscale pore walls, (2) the electroactive grains are interconnected and electrically connected to the current collector/substrate because the porous structure extends in three-dimensions, and (3) the pores allow for good electrolyte accessibility to all the electroactive surfaces.[22,49] Previously, mesoporous MoS_2 was fabricated using a hard templating approach with sacrificial silica templates.[50] In that study, the four-electron conversion reaction was investigated, and stable performance was demonstrated for 100 cycles. However, conversion reactions tend to severely damage the carefully designed nanostructure, making it difficult to correlate performance with morphology.

In this work, we fabricate ordered mesoporous MoS_2 (mp-MoS_2) thin film electrodes to study their pseudocapacitive properties. These mesoporous thin films form an ideal electrode architecture in which the pores provide electrolyte access to the bulk of the film, and the thin nanocrystalline walls are ideal for pseudocapacitive charge storage. The thin film format was also chosen to eliminate the need for conductive carbon additives or binders in order to isolate the effects of nanostructuring the MoS_2.[51]

The mesoporous MoS_2 thin films were synthesized by a two-step method. In the synthesis of these materials, we utilized evaporation induced self-assembly (EISA) of a block copolymer and a sol–gel type precursor to form mesoporous MoO_2 thin films. The films are then converted into MoS_2 using thermal sulfurization. Block copolymer templating is a well-established method to synthesize a variety of ordered mesoporous oxides with uniform, well-defined pore sizes,[51–58] in both thin film[59,60] and powder formats.[61–63] This preliminary step of creating MoO_2 enables precise control of the nanoscale architecture, however, block copolymer templating cannot be used to directly form sulfides. Therefore, we use thermal sulfurization in H_2S to convert the MoO_2 to MoS_2, which preserves the carefully constructed nanoscale architecture. This two-step synthesis method leads to nanocrystalline MoS_2 domains which are directly connected to each other, minimizing the interfacial resistance that is so problematic in nanoparticle agglomerates. The ability to control the pore size, pore-size distribution, and

Materials
Views
www.MaterialsViews.com

ADVANCED
ENERGY
MATERIALS
www.advenergymat.de

FULL PAPER

pore periodicity, further enables optimized electrolyte diffusion, minimizes the pore volume, and can lead to increased power density.[51–54,64,65] In this report, the mesoporous architecture is correlated with the pseudocapacitive properties using a detailed CV analysis that quantitatively decouples pseudocapacitance and diffusion-controlled contributions to overall charge storage. This analysis results in quantification of pseudocapacitive energy storage, which can in turn be used to understand how nanoscale architecture can be used to optimize materials for high power performance.

2. Results and Discussion

2.1. Materials Characterization

Ordered mesoporous MoS_2 thin films were synthesized through the conversion of mesoporous MoO_2 thin films (mp-MoO_2) utilizing a solid–gas reaction with H_2S gas. Mp-MoO_2 was synthesized by EISA of molybdenum sol–gel precursors and an amphiphilic diblock copolymer [poly(ethylene oxide-block-butylene oxide), PEO-b-PBO]. The diblock copolymer utilized in this study does not tend to form very ordered structures because of polydispersity in block length, but due to its high oxygen content, it can be fully removed in the reducing atmospheres needed to crystallize mp-MoO_2 without forming MoO_3.[66] During the solution phase of the sol–gel reaction, the metal chloride precursors undergo condensation reactions catalyzed by in situ generated HCl.[67] The multivalent metal clusters of the molybdenum–oxygen condensates can associate with the electron rich oxygen moieties in the PEO block of the copolymer in solution.[68] During the dip-coating process, solvent evaporation leads to micelle assembly and the formation of inorganic/organic mesostructured composites.[69–73] Thermal

processing can then be used to remove the organic component, leaving a nanoporous network.

Figure 1a shows a scanning electron microscope (SEM) image of a calcined mp-MoO_2 film; the surface of the films presents an ordered porous structure with ≈10 nm pores and ≈10 nm walls. The SEM and transmission electron microscope (TEM) images in Figure 1b,c then show the structure of the mp-MoS_2 that was produced from the mp-MoO_2 by thermal sulfurization in H_2S gas. While the pore walls have clearly increased in thickness due to the lower density of MoS_2 compared to MoO_2, the porosity remains unchanged. The TEM image in Figure 1c further confirms the 3D nature of the pores. Raman spectroscopy (Figure S1, Supporting Information) shows very little scattering from amorphous or graphitic carbon, confirming that the majority of the PEO-b-PBO was removed during the thermal processing. The conversion of the mp-MoO_2 into crystalline mp-MoS_2 is further verified by high resolution TEM (HRTEM) (Figure 1d), which shows S–Mo–S trilayers that can be clearly distinguished as stripe-like patterns. The MoS_2 grains appear to coarsen slightly during the thermal sulfurization, but conversion below 500 °C led to amorphous MoS_2 that did not show pseudocapacitive charge storage behavior. Despite the increase in wall thickness, the overall mesoporous structure is well retained throughout the sulfurization process, suggesting that this synthesis method could be utilized to produce a broad range of nanostructured metal sulfides based on metal oxides that possess desired nanoarchitectures.

Several reports have shown that for carbonaceous supercapacitors, the pore size and size distribution directly affect electrochemical properties.[74–78] Therefore, we have utilized both low angle X-ray diffraction and porosimetry methods to quantify the nature of the porosity. The synchrotron-based grazing incidence small angle scattering (GISAX) (Figure 1 e,f) shows X-ray diffraction arcs along the q_{xy} direction indicating that these thin
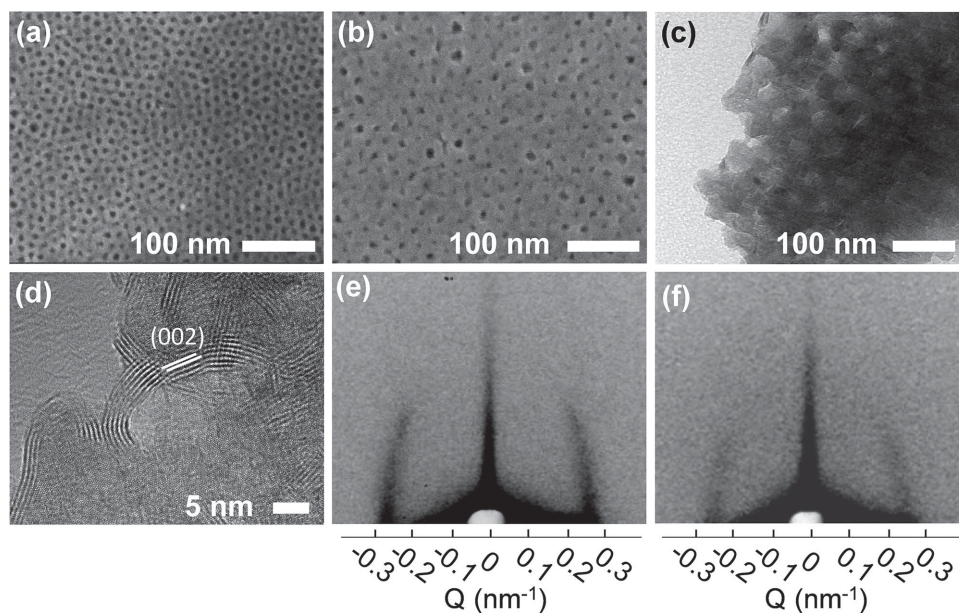

Figure 1. Nanoscale structural characterization. SEM images of the surface of a) a mp-MoO_2 film and b) a mp-MoS_2 thin film. c) TEM image of mp-MoS_2 illustrating the ordered mesoporosity. d) HRTEM of a mp-MoS_2 film showing the (00l) lattice planes. Synchrotron-based 2-D grazing incidence small angle X-ray scattering (GISAX) patterns for e) MoO_2 and f) MoS_2 thin films.
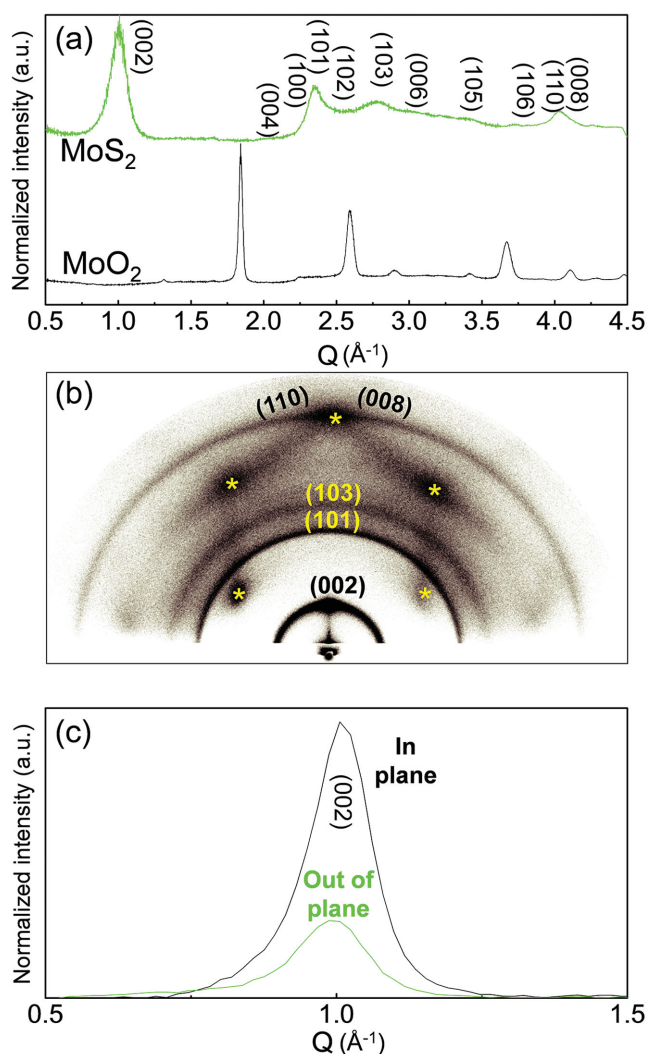
Figure 2. a) Integrated synchrotron based grazing incidence wide angle X-ray scattering (GIWAX) pattern obtained on MoO₂ and MoS₂. b) An example of the raw 2D GIWAX data for the mp-MoS₂ sample. Diffraction rings are indexed on the pattern and the spots marked with an * arise from the silicon substrate. c) Integrated slices of the mp-MoS₂ (002) peaks obtained by integrating over a 10° wedge centered at either 90° or 180° to show the in-plane and out-of-plane diffraction contributions. The data show preferential ordering of the (002) planes parallel to the substrate.

films have ordered porosity in the plane of the substrate. The in-plane repeat distance calculated from q_{xy} (when $q_z \rightarrow 0$) in Figure 1e is 0.28 nm^{-1} or 22 nm in real space. After conversion to mp-MoS₂, this value remains the same, with only a slight diminution of scattering intensity (Figure 1f), as expected for a film that is covalently bound to the substrate. Ellipsometric porosimetry was used to calculate the film thickness and to demonstrate that the porosity observed by SEM on the film surface is homogeneous throughout the bulk of the film. The measured thicknesses of the mp-MoO₂ and the mp-MoS₂ films were determined to be 57 and 85 nm, respectively. Figure S2a,b (Supporting Information) shows toluene adsorption/desorption isotherms for both mp-MoO₂ and mp-MoS₂, respectively.

The mp-MoO₂ and mp-MoS₂ isotherms exhibit a large hysteresis between adsorption and desorption of toluene, which is indicative of a mesoporous structure with a cage and neck-type architecture. Figure S2c,d (Supporting Information) shows the pore size distributions calculated from both the adsorption and desorption branch of the isotherms. Using the adsorption isotherm, the average pore radius of the mp-MoO₂ thin film is calculated to be 8 nm (Figure S2c, Supporting Information) which decreases to 5 nm after conversion to mp-MoS₂ (Figure S2d, Supporting Information). The decrease in pore size and increase in film thickness after conversion to the sulfide can be attributed to a change in density of MoO₂ (density = 6.5 g cm^{-2}) compared to MoS₂ (density = 5.1 g cm^{-2}).

The crystal structure and texture of mp-MoO₂ and the converted mp-MoS₂ were determined using synchrotron-based grazing incidence wide angle X-ray scattering (GIWAX). **Figure 2**a shows that the 1D GIWAX patterns, integrated from the 2D images (Figure S3, Supporting Information), of MoO₂ and MoS₂ match JCPDS No. 32-0671 and JCPDS No. 37-1492, respectively. Scherrer analysis of the (002) planes indicate that mp-MoS₂ grains have a 4 nm coherence length. The small size likely results from a combination of finite size effects, disorder of the van der Waals gaps, and curvature of the (002) planes as observed from the HRTEM in Figure 1d. Due to the relatively low synthesis temperature used here, it seems reasonable that all the layers will not order uniformly along the c-axis direction due to the weak bonding in that direction. We believe that some aspects of the pseudocapacitive charge storage process discussed later in this paper stem from the very small disordered nanoparticles that comprise the pore walls.

Beyond crystallite size effects, the 2D GIWAX (Figure 2b) indicates that mp-MoS₂ exhibits significant texture, with the (002) diffraction planes oriented parallel to the plane of the substrate. To quantify the percent orientation, sections of the 2D GIWAX pattern that correspond to the in-plane direction and out-of-plane scattering direction were integrated separately. The result, shown in Figure 2c, illustrates that the out-of-plane (002) scattering intensity (i.e., scattering from (002) planes oriented parallel to the substrate) is four-times larger than scattering from the in-plane direction (i.e., for (002) planes oriented perpendicular to the substrate). The preferential orientation is highly beneficial for fast intercalation reactions in mp-MoS₂ because bulk ion insertion occurs in the (002) planes rather than through the basal planes.[26] Therefore, the orientation of the mp-MoS₂ crystallites leads to a high density of active edge sites being exposed to the pore volume and thus to the electrolyte. A previous study proposed that iso-oriented mesoporous MoO₃ thin films exhibited fast charge storage kinetics partly because ions easily enter the van der Waals gaps from the pore edges and because this texture helped accommodate electrochemically induced volume expansion normal to the substrate.[51]

2.2. The Electrochemically Driven Semiconductor to Metal Phase Transition

Previous in situ X-ray diffraction (XRD) studies confirmed that upon Li-intercalation, MoS₂ undergoes an irreversible first-order

www.MaterialsViews.com

**ADVANCED
ENERGY
MATERIALS**
www.advenergymat.de

FULL PAPER

phase change from the semiconducting 2H-MoS$_2$ phase to the metallic 1T-MoS$_2$ phase, which is associated with a voltage plateau at 1.1 V versus Li/Li$^+$.36 In the mp-MoS$_2$ system, the CVs shown in **Figure 3**a display a prominent redox peak at 1.1 V versus Li/Li$^+$. After 10 cycles, this electrochemical process at 1.1 V versus Li/Li$^+$ is replaced by a new current response between 1.5–2.5 V versus Li/Li$^+$, which appears during both oxidation and reduction. The broad current response that was observed between 1.5–2.5 V versus Li/Li$^+$ during the first one-hundred cycles becomes more defined, and these new peaks are consistent with lithiation and delithiation of 1T-MoS$_2$[79]

To confirm that this electrochemically driven phase transition is indeed occurring in our mesoporous MoS$_2$ sample, we have combined a number of different techniques to characterize our samples after fifty cycles with a goal of correlating the electrochemical signatures of a phase transition to changes in structure and conductivity. The selected area electron diffraction (SAED) patterns of the pristine and cycled mp-MoS$_2$ films are presented in Figure 3b, and they clearly show diffraction rings that correspond to different crystalline phases. The SAED patterns were integrated, so that the changes could be more clearly distinguished and compared. Figure 3c again shows a clear change in peak position after cycling, and we have ruled out that the cycled MoS$_2$ diffraction pattern is just simply linearly shifted to higher Q by confirming that the two patterns are not superimposable (not shown). In order to give confidence to our collection and processing methods we have simulated the MoS$_2$ 2H pattern, and shown that it is in excellent agreement with both the 1D SAED data and the previously shown GIWAX pattern (Figure 3d). We also simulated the MoS$_2$ 1T pattern using the isostructural CdI$_2$ structure type.[26] This simulated 1T pattern is compared to the integrated pattern obtained from the cycled film and is shown in Figure 3e. The cycled MoS$_2$ agrees fairly well with the simulated pattern, and previous reports;[80–82] however, there is a discrepancy in a few of the peaks, possibly due to some residual Li$^+$ in the 1T lattice, a small amount of 2H material in the sample (see below), or simply to material disorder. It is clear however, that cycling converts the mp-MoS$_2$ into a distinctly different crystalline phase. This electrochemical-driven structural transformation has been shown to lead to a reorganization of the original semiconducting band structure, ultimately leading to metallic conductivity.[80,83]

The structural transformation was further characterized by both X-ray photoemission spectroscopy (XPS) and Raman spectroscopy. High resolution XPS traces for Mo 3d and S 2p confirm the 2H to 1T phase transition (Figure S4, Supporting Information).[84–86] The high resolution Mo 3d spectrum indicates that the molybdenum in mp-MoS$_2$ is in the 4+ valence
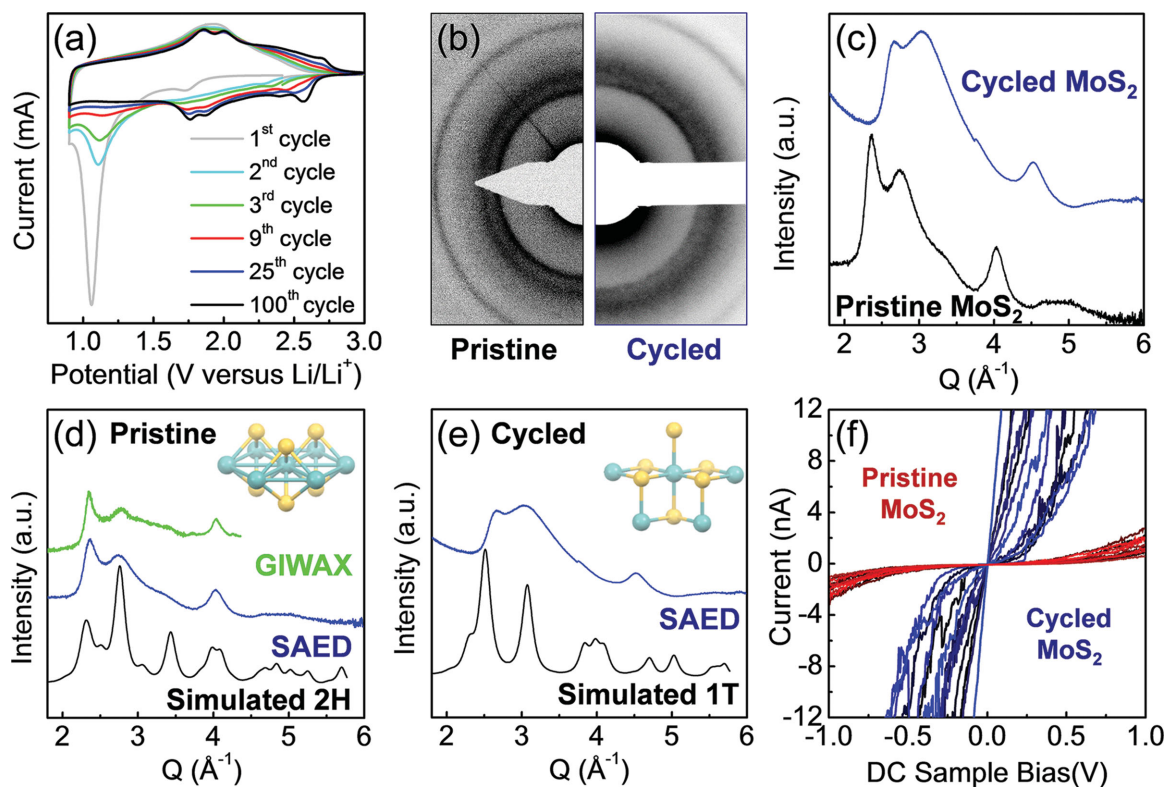

Figure 3. Structural, electrochemical, and electronic characterization of the lithium-driven semiconductor-to-metal phase conversion. a) CVs collected at 5 mV s^{-1} over the first 100 cycles for a mp-MoS$_2$ film. This precycling drives the 2H to 1T phase transition. b) SAED of pristine and cycled mp-MoS$_2$. The diffuse rings are a result of many different crystallite orientations in the selected sample area. c) A clear difference in peak position is observed, both in the raw data and in the 1D patterns obtained by integrating the 2D SAED patterns. d) The pristine mp-MoS$_2$ phase can be identified as 2H-MoS$_2$ by comparison of a 2H simulated powder pattern with both the SAED-derived powder pattern and the GIWAX pattern, all of which are shown in panel (d). e) Reasonable agreement is also observed between the simulated 1T powder pattern and the SAED-derived diffraction pattern obtained on cycled mp-MoS$_2$ in panel (e), further confirming the phase transition. f) I–V curves obtained with current sensing AFM. The current response is dramatically increased in the 1T phase compared to the 2H phase, as expected for a transition from a semiconductor to a metallic conductor.

FULL PAPER

state while the sulfur is in the 2– valence state, both of which are consistent with the electronic structure of MoS₂. Before the phase transformation occurs, the Mo $3d_{5/2}$ signal is best fit to a single peak at 229.4 eV. After the phase transition occurs, the Mo $3d_{5/2}$ peak can be deconvoluted into two independent peaks corresponding to the 2H (229.4 eV) and the 1T phase (228.6 eV).[84–86] We note that the fraction of 2H signal in the converted material is not necessarily representative of the bulk 2H fraction. XPS is a highly surface sensitive method; while the 1T phase is kinetically stable, it is not the thermodynamically stable phase without Li⁺ present, so some back transformation at the material surface is likely. Finally, the local bonding structure of MoS₂ was examined using Raman spectroscopy (Figure S5, Supporting Information), which also confirms the 2H to 1T phase transformation after cycling through the appearance of several new Raman modes.[85,87] While the diffraction data alone does not unequivocally assign the cycled material to the 1T phase, the results of the XPS, Raman, and SAED taken together lead to the clear conclusion that this material is dominantly in the 1T phase after cycling.

While the crystal structure of the new phase is of academic interest, the important question for device performance is the conductivity of the cycled MoS₂. Using current sensing atomic force microscopy (AFM) we have determined that the newly formed phase is much more conductive than the uncycled material, which is expected from the conversion of a semiconductor to a metal. The I–V curves in Figure 3f, obtained in several different locations on the film, show the contrast between the poor conductivity of the semiconducting pristine MoS₂ (red curves) and the metallic conduction of the cycled MoS₂ (black and blue curves). We note, however, that there is variation in the conductivity throughout the cycled film, seen as the spread of curves in Figure 3f. Some of the I–V curves show a sigmodal shape, which is probably due to conduction through a mixture of both 2H and 1T phases. Due to the ex situ nature of this experiment there is a possibility that some of the 1T phase converts back to the 2H phase.

The effect of the increase in electronic conductivity on the charge transfer resistance at the electrode–electrolyte interface was further investigated using electrochemical impedance spectroscopy (EIS). The charge transfer resistance (R_{ct}) can be quantified by fitting the Nyquist plots shown in **Figure 4**a using an appropriate model. We found that at 1.0 V versus Li/Li⁺, R_{ct} is characterized by three distinct regions (Figure 4b). In the first region (cycles 1 and 2) R_{ct} increases, most likely due to solid electrolyte interface (SEI) formation. In the second region (between cycles 2–10), R_{ct} linearly decreases, most likely due to the 2H to 1T phase change. Finally in the third region, between cycles 10–20, R_{ct} begins to stabilize after the phase change is largely completed. Regions two and three of the EIS data correlate well with the CV data presented in Figure 3a, as the electrochemical signature corresponding to the 2H to the 1T phase change occurs predominantly over the first ten cycles.

Finally, structural stability was examined after galvanostatic cycling to determine if the porous architecture and S–Mo–S layer structure were retained after the 2H to 1T phase transformation had occurred. Ex situ GISAX and TEM data (**Figure 5**a,b) collected on mp-MoS₂ after ten Li-ion insertion and deinsertion cycles was used to assess the retention of the ordered
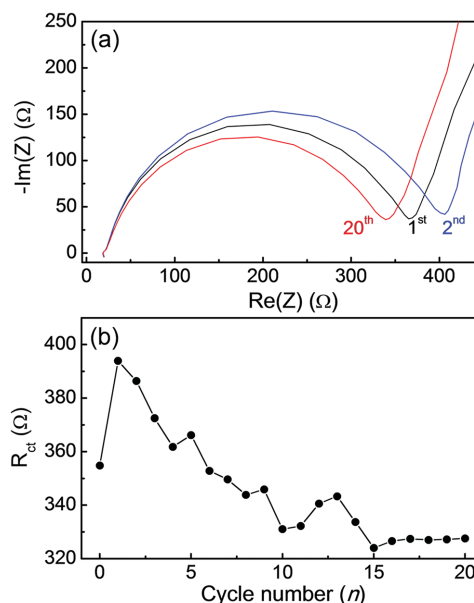

Figure 4. Electrochemical impedance of mp-MoS₂ in a Li-ion electrolyte. a) Nyquist plots of the 1st, 2nd, and 20th cycle collected at 1.0 V versus Li/Li⁺. b) The charge transfer resistance calculated from the mid-frequency intercept of the Nyquist plots over 20 cycles. The charge transfer resistance increases after the first Li-ion insertion process, most likely due to SEI formation. It then decreases with further cycling, finally stabilizing after 15 cycles.
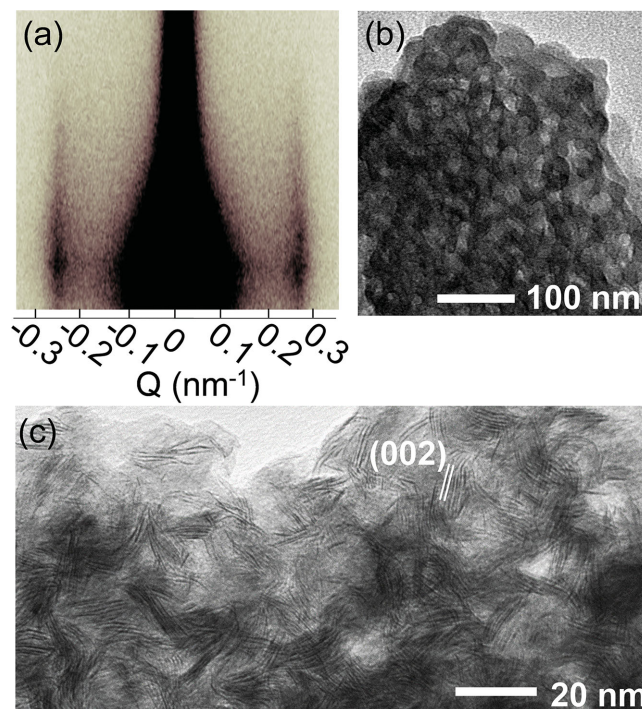

Figure 5. Structural characterization after the 2H to 1T phase transition. a) GISAX pattern, b) TEM image, and c) HRTEM image of the mp-MoS₂ after cycling. The data show excellent retention of the ordered mesoporous structure, and layered atomic structure, even after the Li-ion induced 2H-to-1T phase change.

mesoporosity of mp-MoS$_2$. The data in Figure 5a establishes that the low angle X-ray scattering from the cycled pore system is nearly identical to that of the uncycled material. TEM also confirms that the newly formed 1T MoS$_2$ phase looks very much like the original 2H material on the nanometer length scale. Finally, HRTEM (Figure 5c) shows that the stripe-like S–Mo–S layers are preserved, a fact that is central to the fast pseudocapacitive charge storage that will be discussed in the next section.

2.3. Electrochemistry

In this section, we will examine the fundamental electrochemical properties of the 1T-phase of mp-MoS$_2$. The metallic conductivity of 1T-MoS$_2$ in combination with the interconnected grains is highly beneficial for fast charge transfer reactions. CVs collected between 1–100 mV s^{-1} for 1T mp-MoS$_2$ are shown in **Figure 6**a,b. Clear redox peaks are observed between 1.7 and 2.6 V versus Li/Li$^+$, and broad distribution of redox current is measured between 1.0–1.7 V versus Li/Li$^+$. Similar redox peaks are observed in slurry electrodes made from micron-sized MoS$_2$ powders (Figure S6, Supporting Information), but these bulk electrodes show a low current response below 1.75 V versus Li/Li$^+$. Therefore, we attribute this new electrochemical process

in our mp-MoS$_2$ to the porous architecture that leads to a high density of easily accessible surface-redox active sites. These surface sites will be highly defective in nature and most likely will have a broad distribution of energies associated with oxidation and reduction. A similar broadened electrochemical signature is observed in RuO$_2$ .xH$_2$O[15] which is ascribed to pseudocapacitive charge storage.

The peaks in the CVs (Figure 6a,b) ≈1.5–2.0 V show relatively little change in potential as a function of sweep rate. This indicates rapid Li-ion insertion/deinsertion kinetics in our mp-MoS$_2$. The total charge storage in the mp-MoS$_2$ is plotted as a function of charge time in Figure 6c; the data indicates that the maximum value for the gravimetric capacity, 173 mAh g^{-1}, is reached after 2000 s. This capacity is in reasonable agreement with the theoretical value of 167 mAh g^{-1} for the insertion of one Li$^+$ per MoS$_2$. The small additional capacity over theoretical is likely due to the presence of new surface redox sites. More significant, however, is that 140 mAh g^{-1} or over 80% of the theoretical capacity can be obtained in just 20 s. Galvanostatic measurements were also performed to complement the CV measurements (Figure S7, Supporting Information). The pseudolinear galvanostatic traces clearly distinguish this charge storage mechanism from battery-type or diffusion dominated charge storage. Similar charge storage kinetics are observed in
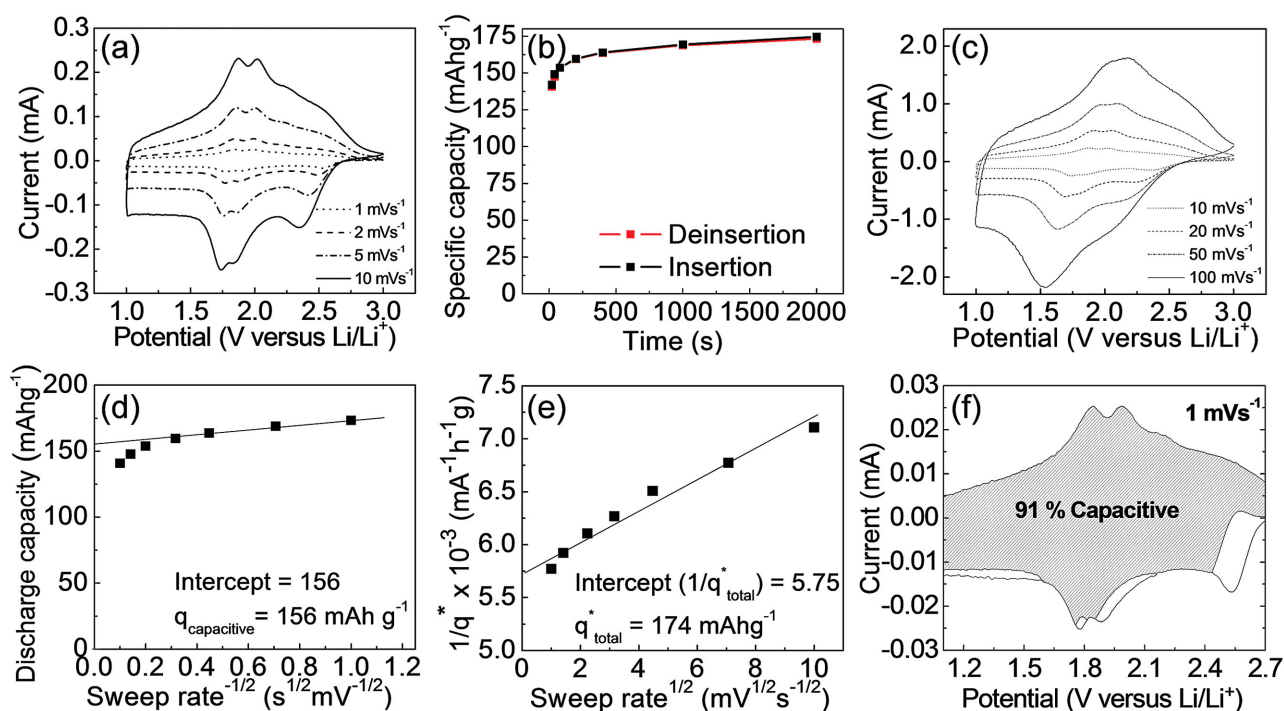

Figure 6. Electrochemical characterization of mp-MoS$_2$ collected using Li-ion electrolytes. a) CVs collected at scan rates ranging from 1–10 mV s^{-1}. b) CVs collected at scan rates ranging from 10–100 mV s^{-1}. c) Specific capacity versus charge and discharge time. d,e) Trasatti analysis utilizing the dependence of voltammetric charge storage on the sweep rate. d) As $\upsilon \to \infty$ access to the more diffusion-controlled redox sites are excluded and extrapolation of capacity versus $\nu^{-1/2}$ gives the capacitive charge storage ($q_{capacitive}$), which is calculated to be 156 mAh g^{-1}. e) As $\upsilon \to 0$ access to the diffusion limited redox sites can occur and so extrapolation of the inverse capacity versus $\nu^{1/2}$ gives the extrapolated total charge (q_{total}), which is calculated to be 174 mAh g^{-1}. Using the relationship $q_{total} = q_{capacitive} + q_{diffusion}$, we can conclude that our $q_{diffusion}$ is 18 mAh g^{-1} indicating that the majority of the charge storage occurs in a nondiffusion controlled manner in our mp-MoS$_2$. The ratio of the capacitive charge storage to the total charge storage is 90%. f) Capacitive and diffusion-controlled charge storage contributions for mp-MoS$_2$ cycled in a Li-ion electrolyte at 1 mV s^{-1} can also be calculated using the method described in Equation (3). The capacitive contribution is 91% and is denoted by the shaded grey region; these results are thus in good agreement with the Trasatti analysis.

both the CV and galvanostatic measurements, as expected for a capacitive system. The voltage drop at high C-rates is small and comparable to the small peak position hysteresis observed in the CV measurements. We propose that the fast kinetics are due to the metallic conductivity of mp-MoS$_2$ combined with an ideal nanoscale architecture consisting of interconnected nanocrystals with short ion diffusion path lengths and good electrolyte accessibility. The performance metrics are extremely high when compared to other oxide pseudocapacitors.[88,89]

To further explore the nature of these charge storage processes, the electrochemical insertion/deinsertion kinetics of mp-MoS$_2$ were investigated using the Trasatti analysis[90–92] to quantify the diffusion-controlled and capacitive charge storage processes

$$q(v) = q_{capacitive} + \alpha \left(v^{-1/2} \right) \quad (1)$$

$$\frac{1}{q(v)} = \frac{1}{q_{tot}} + \alpha \left(v^{1/2} \right) \quad (2)$$

where $q(v)$ is the total measured voltammetric charge transfer, $q_{capacitive}$ refers to capacitive charge storage (both from double layer and pseudocapacitive processes), q_{tot} is the total amount of charge storage, and $\alpha v^{-1/2}$ indicates charge storage associated with semi-infinite diffusion, where α is a constant and v is the sweep rate. Utilizing Equation (1), as $v \to \infty$, access to the more diffusion-controlled redox sites are excluded and the intercept of the extrapolated capacity versus $v^{-1/2}$ trend line gives the capacitive charge storage ($q_{capacitive}$), which is calculated to be 156 mAh g^{-1}. On the other hand, utilizing Equation (2), as $v \to 0$, the electrochemical reaction time-scale is long enough to allow access to all sites in the material and extrapolation of $\frac{1}{q(V)}$ versus $v^{1/2}$ gives the extrapolated total charge (q_{tot}), which is calculated to be 174 mAh g^{-1} (Figure 6e), in excellent agreement with the highest capacity we obtained at 2000 s. The ratio of the capacitive charge storage to the total charge storage is 90%, which is extremely high, and intimately related to the unique nanoscale architecture of this material.

A second analysis was also performed to determine the potential regions where capacitive contributions occur in the CV plots. The measured current response as a function of potential is considered to be comprised of both capacitive currents (which vary as k_1v) and diffusion-controlled currents (which vary as $k_2v^{1/2}$), as given in Equation (3)

$$i(V) = k_1 v + k_2 v^{1/2} \quad (3)$$

Here 'i (V)' is the measured current as a function of potential '(V)', and 'v' is the scan rate.

Figure 6f shows this kinetic analysis at a sweep rate of 1 mV s^{-1}. Such a slow sweep rate is preferred for this analysis in order to provide the conditions which maximize the diffusion contribution. The analysis indicates that some 91% of the current, and therefore the capacity, is capacitive, which is in excellent agreement with the Trasatti analysis. The kinetic analysis reveals that the insertion processes, especially in the voltage region ≈2.55 V, is more diffusion controlled than the deinsertion process. Reports have suggested that the electrochemically produced 1T
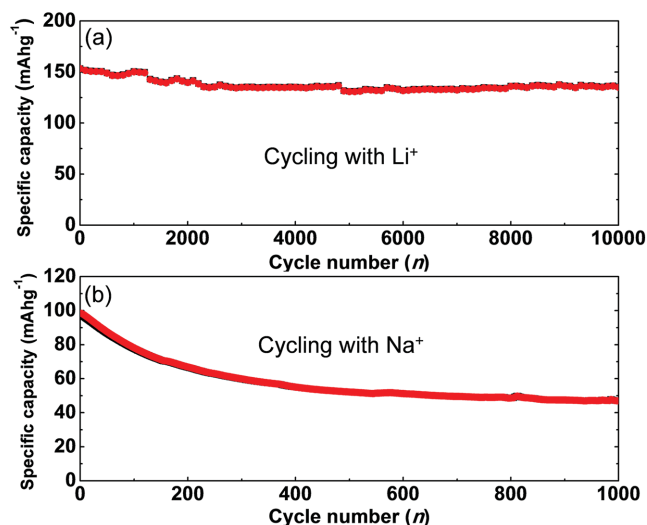

Figure 7. Long-term cycling stability. a) Specific capacity versus cycle number for a mp-MoS$_2$ film cycled galvanostatically at 23 C in a Li-ion electrolyte. b) Specific capacity versus cycle number for a mp-MoS$_2$ film cycled potentiostatically at 10 mV s^{-1} in a Na-ion electrolyte.

phase can convert back to a disordered 2H-phase at 3 V by a glide-plane sliding mechanism of the sulfur layers.[36] If there is a sliding of sulfur layers concomitant with deintercalation (oxidation) at 2.55 V, then diffusion-controlled charge storage processes may occur upon reintercalation (reduction) because of the need to reverse this partial back transition. Overall, however, this kinetic analysis indicates that almost all of the charge storage in mp-MoS$_2$ is capacitive throughout the entire voltage range measured. The capacity must come from surface-redox processes combined with intercalation over short diffusion path lengths (intercalation pseudocapacitance).[51] Because the different processes are all kinetically facile, the contributions from surface, near surface, and 'interior' redox processes cannot be distinguished from one another. We postulate that the ideal 3D porous geometry, combined with preferentially oriented nanocrystals produce an environment suitable for this high degree of capacitive charge storage.

Our final set of lithium intercalation experiments address the question of cycling stability. Fast redox reactions and high levels of pseudocapacitive charge storage generally indicate minimal structural change upon lithium intercalation. This, in turn, provides the potential for increased cycling stability. Indeed, **Figure 7**a shows that mp-MoS$_2$ can be cycled 10 000 times at a rate of 23 C (2.5 min charge) with a loss in capacity of only 13%. The voltage versus capacity plots shown in Figure S8 in the Supporting Information demonstrate extremely good stability of this electrochemical charge storage process. We ascribe this excellent cycling behavior to the robust nanostructure and oriented crystal structure of mp-MoS$_2$. The orientation of the (002) planes (Figure 2c) should lead to iso-oriented volume expansion normal to the substrate during cycling, which in turn, decreases cycling induced strain. In addition, the flexible porous network should be able to accommodate any cycling induced volume changes by allowing the material to expand and contract without loss of connection to the current collector or neighboring MoS$_2$ grains.[51] To confirm these ideas, the structural stability of the
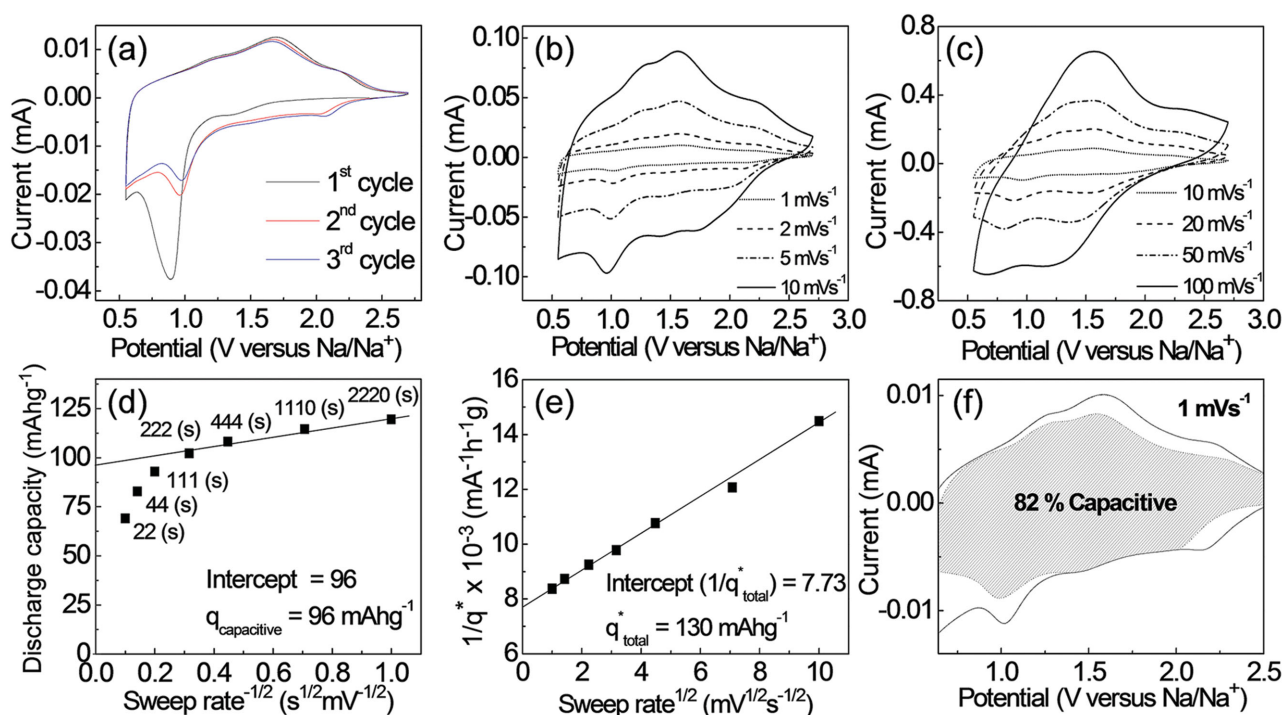
Figure 8. Electrochemical characterization of mp-MoS$_2$ collected using Na-ion electrolyte. a) CVs collected at 5 mV s^{-1} for the first three cycles. b) CVs collected at scan rates ranging from 1–10 mV s^{-1}. c) CVs collected at scan rates ranging from 10–100 mV s^{-1}. d,e) Trasatti analysis utilizing the dependence of voltammetric charge storage on the sweep rate. d) As $\upsilon \to \infty$, access to the more diffusion-controlled redox sites are excluded and extrapolation of capacity versus $\upsilon^{-1/2}$ gives the capacity charge storage ($q_{capacitive}$), which is calculated to be 96 mAh g^{-1}. e) As $\upsilon \to 0$, access to the diffusion limited redox sites can occur and so extrapolation of the inverse capacity versus $\upsilon^{1/2}$ gives the extrapolated total charge (q_{total}), which is calculated to be 130 mAh g^{-1}. Using the relationship $q_{total} = q_{capacitive} + q_{diffusion}$, we can conclude that $q_{diffusion}$ is 34 mAh g^{-1} and the ratio of the capacitive charge storage to the total charge storage is 74%. f) Capacitive and diffusion-controlled charge storage contributions for mp-MoS$_2$ cycled in a Na-ion electrolyte at 1 mV s^{-1} can also be calculated using the method described in Equation (3). The capacitive contribution is 82% and is denoted by the shaded grey region; these results are thus in good agreement with the Trasatti analysis.

mp-MoS$_2$ was examined after 10 000 cycles by Raman spectroscopy (Figure S9, Supporting Information) and XPS (Figure S10, Supporting Information). Both measurements indicate that the 1T phase is still predominantly present. More importantly, the TEM image confirms that the porous nanoscale architecture is preserved (Figure S9, Supporting Information).

We next turn our discussion to the pseudocapacitive charge storage properties of Na-ion insertion in mp-MoS$_2$. We emphasize again that we are focusing only on the intercalation of Na$^+$ into mesoporous MoS$_2$ because the four-electron reduction reaction extensively damages the nanoscale architecture of the MoS$_2$. A recent in situ XRD study demonstrated that electrochemical intercalation of up to 1.1 Na-ions per Mo occur in MoS$_2$ powders with micrometer size dimensions.[38] The electrochemical intercalation of Na-ions should be slower in MoS$_2$, compared to Li-ion intercalation, because of the larger ionic radius of Na$^+$ (r_{ionic} = 1.06 Å) versus Li$^+$ (r_{ionic} = 0.76 Å).[93,94] Nonetheless, MoS$_2$ is an ideal candidate to accommodate a larger guest ion like Na$^+$ because the large van der Waals gaps have been shown to intercalate guest ions and molecules even larger than Na$^+$.[26]

Similar to Li-ion insertion into MoS$_2$, Na-ion insertion into MoS$_2$ also induces a phase change from the 2H phase to the metallic 1T phase.[95] The large current response at 0.90 V versus Na/Na$^+$ in **Figure 8**a corresponds to conversion into the 1T-MoS$_2$ phase.[95] With further cycling this peak at 0.90 V decays while

new broad peaks appear between 1.25–2.25 V versus Na/Na$^+$. After the phase transition was completed, CVs were collected between 1–100 mV s^{-1} as shown in Figure 8b,c. Figure 8d shows that the magnitude of Na-ion charge storage is not as large as the Li-ion storage as now the total charge storage after an extended period of time (2200 s) is only 118 mAh g^{-1}, about 80% of the theoretical value of 146 mAh g^{-1}. Not surprisingly, the kinetics are also slower than for Li ions as less than 50% of the theoretical capacity (69 mAh g^{-1}) can be accessed in the 20 s time frame. Similar to the analyses performed on the Li-ion storage mechanism, the Na-ion charge storage properties were examined using these same methods. Utilizing Equation (1), the intercept of the extrapolated capacity versus $\upsilon^{-1/2}$ trend-line gives the capacitive charge storage ($q_{capacitive}$), which is calculated to be 96 mAh g^{-1} (Figure 8d). On the other hand, utilizing Equation (2), the extrapolation of $\frac{1}{q(V)}$ versus $\upsilon^{1/2}$ gives the extrapolated total charge (q_{tot}), which is calculated to be 130 mAh g^{-1} (Figure 8e). Unlike the Li$^+$ case, this value is slightly larger than the capacity we measured at 1 mV s^{-1}, most likely because the larger Na-ions are more limited by diffusion than the smaller Li-ions, so an even slower sweep rate would be required to experimentally obtain a value equal to q_{tot}. Using these values, the ratio of the capacitive charge storage to the total charge storage is 74%, which is extremely high for this larger

FULL PAPER

cationic species. Utilizing Equation (3) (Figure 8e), we find that 82% of the stored charge arises from nondiffusion-controlled or capacitive processes, which is in very good agreement with the Trasatti analysis. This result emphasizes that the large MoS_2 van der Waals gaps form ideal diffusion pathways that promote a capacitor-like charge storage mechanism, even with the larger Na-ions. The cycling stability of mp-MoS_2 in a Na-ion electrolyte is not as good as that for Li-ions (Figure 7b). After 100 cycles the capacity has dropped to only 80% of the original value and the capacity eventually stabilizes at around 50% of the original value. The system can achieve more than 1000 cycles at this 50% capacity, however.

3. Conclusion

We have demonstrated that 3D ordered porous MoS_2 can be synthesized from polymer templated MoO_2 materials. These MoS_2 thin films possess ideal nanoarchitectures for pseudocapacitive energy storage. The 10 nm pore walls provide short ion diffusion path lengths, while the pore voids allow good electrolyte accessibility to the electrochemically active walls. During the preliminary conditioning cycles, the semiconducting 2H-phase of MoS_2 is converted into the metallic 1T-phase of MoS_2 through intercalation of alkali metals. This transition was confirmed using AC impedance spectroscopy, electron diffraction, Raman spectroscopy, and XPS. Using current sensing AFM, we report a dramatic increase in conductivity as a result of the structural transition. The increased electronic conduction is only amplified in this 3D porous geometry because the MoS_2 grains are interconnected. Ex situ GISAX and TEM confirm that the electrochemically formed 1T phase possessed the same mesoscale structure as the as-synthesized parent 2H-MoS_2 material. Synchrotron-based GIWAX was used to analyze the texture of the MoS_2 crystal structure and revealed that the (002) planes are oriented parallel to the substrate. This orientation leads to a high degree of MoS_2 edge sites that form the interior of the pore walls and are in direct contact with the electrolyte.

The combination of these structural factors leads to the extremely fast kinetics. For Li-ions, over 80% of the theoretical capacity can be accessed in only 20 s, which is consistent with the analysis indicating that a high percentage of the charge storage is capacitor-like. Moreover, the cycling performance is extremely good as the capacity decrease over 10 000 cycles is only 13%. The charge storage properties for the larger Na-ions are also quite respectable. For this ion, about 50% of the theoretical capacity is stored on the 20 s time frame, and here, too, most of the charge storage is capacitor-like. Overall, we have demonstrated that mp-MoS_2 is a versatile ion storage host that is capable of achieving fast kinetics and good cycling performance. We foresee that these unique structural properties may eventually give rise to possible pseudocapacitive storage with an even larger library of guests, including higher valent ions such as Ca^{2+} and Mg^{2+}.

4. Experimental Section

Materials: The following materials were obtained from commercial suppliers and used without further purification: Molybdenum(V) chloride

(99.6% metal basis, Alfa Aesar), PBO(5000)-b-PEO(6500), M_n = 11 500, Polydispersity Index (PDI) = 1.06–1.15, Advanced Polymer Materials Inc).

Synthesis of MoO_2: In a typical synthesis, 0.015 g PEO-b-PBO was first dissolved in 2 mL ethanol. Then, 0.2 g $MoCl_5$ was added. The resulting solution was stirred for 2 h prior to film deposition. Thin films were deposited via dip-coating on polar substrates such as silicon and platinum-coated Si (3 nm Ti-150 nm Pt- 360 nm SiO_2- Si). Optimal conditions included 4% relative humidity and a constant withdrawal rate of 3 mm s^{-1}. The films were aged at 180 °C for 12 h prior to template removal to prevent loss of mesoscale order during the course of the thermal template degradation and crystallization. The films were calcined using a 1 °C min^{-1} ramp to 350 °C in a 5%/95% H_2/N_2 reducing atmosphere to yield the crystalline, porous MoO_2.

Synthesis of MoS_2: The (above) as synthesized MoO_2 thin-films were converted to MoS_2 through a solid–gas reaction with H_2S gas. The reaction was carried out in a tube furnace at 500 °C under flowing H_2S/H_2 (H_2S 5 mol%:H_2 95 mol%, Air Gas) for 3 h. A low gas flow rate of 30 mL min^{-1} was used to minimize thermal gradients across the films. The system was cooled, under H_2S/H_2 flow, at 2–4 °C min^{-1} until 120 °C at which point the flow gas was changed to argon, which was used until the system reached room temperature. The samples were exposed to air for ≈30–60 min before being transferred and stored in a glovebox.

GISAX and GIWAX Synchrotron Measurement: 2D GISAX and GIWAX data were collected at the Stanford Synchrotron Lightsource (SSRL) using beamlines 1–4 and 11–3, respectively. Beamline 1–4 was operated at 8.344 KeV using the Rayonix-165 CCD detector. Beamline 11–3 was operated at 12.735 KeV using a MAR345 imaging plate (345 mm diameter).

Porosimetry: Ellipsometric porosimetry was performed on a PS-1100 instrument from Semilab using toluene as the adsorbate. A UV–vis CCD detector adapted to a grating spectrograph analyzes the signal reflected by the sample. The light source is a 75 W Hamamatsu Xenon lamp and measurements were performed in the spectral range from 1.25–4.5 eV. Data analysis was performed using the associated Spectroscopic Ellipsometry Analyzer software with the assumption of cylindrical pores.

XPS: XPS analysis was performed using a Kratos Axis Ultra DLD with a monochromatic Al Kα radiation source. The charge neutralizer filament was used to control charging of the sample, a 20 eV pass energy was used with a 0.05 eV step size, and scans were calibrated using the C 1s peak shifted to 284.8 eV. The integrated area of the peaks was found using the CasaXPS software, and atomic ratios were also found using this software. The atomic sensitivity factors used were from the Kratos library within the Casa software.

Raman: Raman spectra were obtained using a Renishaw InVia micro-Raman spectrometer equipped with an 1800 lines mm-1 grating, Rayleigh line rejection edge filter, Peltier-cooled deep depletion CCD array detector (576 × 384 pixels). The excitation source used to acquire the spectra was a 514 nm line from an argon ion laser (25 mW) and a 63×/1.2 NA water-immersion objective was used to produce a spot size of ≈1 μm on the sample.

TEM: TEM was performed using an FEI Technai T12 operating at 120 kV. HRTEM images were collected using an FEI Titan S/TEM operating at 300 kV in transmission mode. Selected area electron diffraction patterns were collected on the same instrument in diffraction mode operating at 300 kV with a selected area aperture at 50 μm.

AFM: AFM was carried out in the conductive (cAFM) mode using the Nanoscope V Dimension Icon equipped with the Extended TUNA applications module (Bruker) in ambient conditions. Local I–V spectroscopy employed Pt-coated silicon cantilevers (OSCM-PT-R3, Bruker) with nominal spring constants of 2 N m^{-1}, probe resistance of 350 Ohms, and nominal tip radii of 15 nm in contact mode. The bias voltage was applied to the sample with respect to a virtually grounded cAFM probe tip. Bias voltage sweeps were carried out at the rate of 1 V s^{-1} over the range of interest while maintaining a constant applied force throughout by means of the feedback loop. A minimum applied force was used so as to reduce sample perturbation during the measurement. The I–V characteristics were stable with repeated positive and negative bias sweeps.

Electrochemistry: The as-prepared mp-MoS$_2$ thin films on Pt-coated silicon substrates were used as working electrodes. Electrochemical measurements of these thin film electrodes in both Li-ion and Na-ion electrolytes were carried out in a three-electrode cell. The lithium ion electrochemistry was carried out in 1 M LiClO$_4$ in propylene carbonate with lithium foils used as a counter and reference electrode. The mp-MoS$_2$ thin films were cycled 100 times between 0.8 and 3.0 V (vs Li/Li$^+$) to complete the phase transition to the 1T phase, and then a voltage window between 1.0 and 3.0 V (vs Li/Li$^+$) was used to investigate the capacity and kinetics of mp-MoS$_2$ using an Arbin BT-2000. The films were cycled in galvanostatic mode for the cyclability test with Li. The sodium ion electrochemistry was carried out in 1 M NaClO$_4$ in propylene carbonate, and sodium foils were used as a counter and reference electrode. Cyclic voltammetry was performed between 0.55 and 2.7 V (vs Na/Na$^+$) using a PAR EG&G 273A potentiostat. The mp-MoS$_2$ was cycled 20 times at 1 mV s^{-1} in order to complete the phase change to the 1T phase followed by the kinetic analysis and capacity measurement. All tests were performed in an argon or nitrogen-filled glovebox. Electrochemical impedance spectroscopy was carried out on a VSP potentiostat/galvanostat (Bio-Logic). The impedance measurements were performed between 900 kHz and 100 mHz using a 10 mV amplitude and no bias. Impedance data was collected at 1V (vs Li/Li$^+$) after each insertion and deinsertion cycle. A 5 min potentiostatic hold was applied before each impedance measurement to stabilize the voltage.

Inductively Coupled Plasma Atomic Emission Spectroscopy for Thin Film Mass Determination: After electrochemical cycling in either Li-ion or Na-ion electrolytes, the mp-MoS$_2$ thin films were dissolved in aqua regia (nitric acid:hydrochloric acid = 1:3) for 30 min. The samples were analyzed with a PerkinElmer Optima 7000DV using a GemTip Cross-Flow nebulizer. The calculated areal loading from several films is 36 µg cm^{-2} ± 1µg cm^{-2}, which was used for the determination of the mass normalized capacities in this report.

Supporting Information

Supporting Information is available from the Wiley Online Library or from the author.

Acknowledgements

[1] M. Park, X. Zhang, M. Chung, G. B. Less, A. M. Sastry, *J. Power Sources* **2010**, *195*, 7904.
[2] N. Balke, S. Jesse, A. N. Morozovska, E. Eliseev, D. W. Chung, Y. Kim, L. Adamczyk, R. E. García, N. Dudney, S. V. Kalinin, *Nat. Nanotechnol.* **2010**, *5*, 749.
[3] M. D. Stoller, S. Park, Y. Zhu, J. An, R. S. Ruoff, *Nano Lett.* **2008**, *8*, 3498.
[4] M. F. El-kady, V. Strong, S. Dubin, R. B. Kaner, *Science* **2012**, *335*, 1326.
[5] M. Winter, R. J. Brodd, *Chem. Rev.* **2004**, *104*, 4245.
[6] P. Simon, Y. Gogotsi, *Nat. Mater.* **2008**, *7*, 845.
[7] S. W. Lee, N. Yabuuchi, B. M. Gallant, S. Chen, B.-S. Kim, P. T. Hammond, Y. Shao-Horn, *Nat. Nanotechnol.* **2010**, *5*, 531.
[8] B. E. Conway, *Electrochem. Sci. Technol.* **1991**, *138*, 1539.
[9] B. E. Conway, V. Birss, J. Wojtowicz, *J. Power Sources* **1997**, *66*, 1.
[10] B. E. Conway, W. G. Pell, *J. Solid State Electrochem.* **2003**, *7*, 637.
[11] V. Augustyn, J. Come, M. A. Lowe, J. W. Kim, P. Taberna, S. H. Tolbert, H. D. Abruña, P. Simon, B. Dunn, *Nat. Mater.* **2013**, *12*, 1.
[12] V. Augustyn, P. Simon, B. Dunn, *Energy Environ. Sci.* **2014**, *7*, 1597.
[13] S. Boukhalfa, K. Evanoff, G. Yushin, *Energy Environ. Sci.* **2012**, *5*, 6872.
[14] Y. Shi, L. Peng, Y. Ding, Y. Zhao, G. Yu, *Chem. Soc. Rev.* **2015**, *44*, 6684.
[15] J. P. Zheng, P. J. Cygan, T. R. Jow, *J. Chem. Soc.* **1995**, *142*, 2699.
[16] M. Toupin, T. Brousse, D. Belanger, *Chem. Mater.* **2004**, *16*, 3184.
[17] V. Augustyn, W. Kim, P. Rozier, P. Taberna, P. Gogotsi, J. W. Long, B. Dunn, P. Simon, *J. Chem. Soc.* **2014**, *161*, 718.
[18] E. Lim, H. Kim, C. Jo, J. Chun, K. Ku, S. Kim, H. Lee, I.-S. Nam, S. Yoon, K. Kang, J. Lee, *ACS Nano* **2014**, *8*, 8968.
[19] H.-S. Kim, J. B. Cook, S. H. Tolbert, B. Dunn, *J. Electrochem. Soc.* **2015**, *162*, A5083.
[20] J. Wang, J. Polleux, J. Lim, B. Dunn, *J. Phys. Chem.* **2007**, *111*, 14925.
[21] Q. Wang, Z. H. Wen, J. H. Li, *Adv. Funct. Mater.* **2006**, *16*, 2141.
[22] K. Brezesinski, J. Wang, J. Haetge, C. Reitz, S. O. Steinmueller, S. H. Tolbert, B. M. Smarsly, B. Dunn, T. Brezesinski, *J. Am. Chem. Soc.* **2010**, *132*, 6982.
[23] V. Augustyn, J. Come, M. A. Lowe, J. W. Kim, P. Taberna, S. H. Tolbert, H. D. Abruña, P. Simon, B. Dunn, *Nat. Mater.* **2013**, *12*, 1.
[24] G. A. Muller, J. B. Cook, H.-S. Kim, S. H. Tolbert, B. Dunn, *Nano Lett.* **2015**, *15*, 1911.
[25] M. S. Whittingham, *Chem. Rev.* **2004**, *104*, 4271.
[26] E. Benavente, M. A. S. Ana, F. Mendiza, G. Gonza, *Coord. Chem. Rev.* **2002**, *224*, 87.
[27] Y. Liang, R. Feng, S. Yang, H. Ma, J. Liang, J. Chen, *Adv. Mater.* **2011**, *23*, 640.
[28] H. Hwang, H. Kim, J. Cho, *Nano Lett.* **2011**, *11*, 4826.
[29] T. Stephenson, Z. Li, B. Olsen, D. Mitlin, *Energy Environ. Sci.* **2014**, *7*, 209.
[30] H. Yoo, A. P. Tiwari, J. Lee, D. Kim, J. H. Park, H. Lee, *Nanoscale* **2015**, *7*, 3404.
[31] C. Zhu, X. Mu, P. A. van Aken, Y. Yu, J. Maier, *Angew. Chem., Int. Ed. Engl.* **2014**, *53*, 2152.
[32] X. Fang, C. Hua, X. Guo, Y. Hu, Z. Wang, X. Gao, F. Wu, J. Wang, L. Chen, *Electrochim. Acta* **2012**, *81*, 155.
[33] L. David, R. Bhandavat, G. Singh, *ACS Nano* **2014**, *8*, 1759.
[34] R. R. Haering, J. A. Stiles, K. Brandt, (Moli Energy Ltd) *US Patent 4224309*, **1980**.
[35] F. C. Laman, K. Brandt, *J. Power Sources* **1988**, *24*, 195.
[36] M. A. Py, R. R. Haering, *Can. J. Phys.* **1982**, *61*, 76.
[37] X. Fang, C. Hua, X. Guo, Y. Hu, Z. Wang, X. Gao, F. Wu, J. Wang, L. Chen, *Electrochim. Acta* **2012**, *81*, 155.

[38] J. Park, J.-S. Kim, J.-W. Park, T.-H. Nam, K.-W. Kim, J.-H. Ahn, G. Wang, H.-J. Ahn, *Electrochim. Acta* **2013**, *92*, 427.

[39] F. C. Laman, K. Brandt, *J. Power Sources* **1988**, *24*, 195.

[40] A. Ramadoss, T. Kim, G.-S. Kim, S. J. Kim, *New J. Chem.* **2014**, *38*, 2379.

[41] X. Zhang, C. An, S. Wang, Z. Wang, D. Xia, *J. Cryst. Growth* **2009**, *311*, 3775.

[42] M.-J. Hwang, K. M. Kim, K.-S. Ryu, *J. Electroceram.* **2014**, *33*, 239.

[43] H. Yu, Y. Liu, S. L. Brock, *Inorg. Chem.* **2008**, *47*, 1428.

[44] X. W. Lou, H. C. Zeng, *Chem. Mater.* **2002**, *14*, 4781.

[45] Y. Zhao, Y. Zhang, Z. Yang, Y. Yan, K. Sun, *Sci. Technol. Adv. Mater.* **2013**, *14*, 043501.

[46] S. Wang, C. An, J. Yuan, *Materials* **2010**, *3*, 401.

[47] X. Hu, W. Zhang, X. Liu, Y. Mei, Y. Huang, *Chem. Soc. Rev.* **2015**, *44*, 2376.

[48] Y. Wang, H. Li, P. He, E. Hosono, H. Zhou, *Nanoscale* **2010**, *2*, 1294.

[49] M. Ihsan, Q. Meng, L. Li, D. Li, H. Wang, K. H. Seng, Z. Chen, S. J. Kennedy, Z. Guo, H.-K. Liu, *Electrochim. Acta* **2015**, *173*, 172.

[50] H. Liu, D. Su, R. Zhou, B. Sun, G. Wang, S. Z. Qiao, *Adv. Energy Mater.* **2012**, *2*, 970.

[51] T. Brezesinski, J. Wang, S. H. Tolbert, B. Dunn, *Nat. Mater.* **2010**, *9*, 146.

[52] E. K. Richman, C. B. Kang, T. Brezesinski, S. H. Tolbert, *Nano Lett.* **2008**, *8*, 3075.

[53] T. Brezesinski, M. Groenewolt, N. Pinna, H. Amenitsch, M. Antonietti, B. Smarsly, *Adv. Mater.* **2006**, *18*, 1827.

[54] T. Brezesinski, J. Wang, J. Polleux, B. Dunn, S. H. Tolbert, *J. Am. Chem. Soc.* **2009**, *131*, 1802.

[55] R. Buonsanti, T. E. Pick, N. Krins, T. J. Richardson, B. A. Helms, D. J. Milliron, *Nano Lett.* **2012**, *12*, 3872.

[56] I. E. Rauda, R. Buonsanti, L. C. Saldarriaga-Lopez, K. Benjauthrit, L. T. Schelhas, M. Stefik, V. Augustyn, J. Ko, B. Dunn, U. Wiesner, D. J. Milliron, S. H. Tolbert, *ACS Nano* **2012**, *6*, 6386.

[57] J. M. Feckl, K. Fominykh, M. Döblinger, D. Fattakhova-Rohlfing, T. Bein, *Angew. Chem., Int. Ed.* **2012**, *51*, 7459.

[58] M. C. Orilall, U. Wiesner, *Chem. Soc. Rev.* **2011**, *40*, 520.

[59] Y. Ren, Z. Ma, P. G. Bruce, *Chem. Soc. Rev.* **2012**, *41*, 4909.

[60] Y. Ye, C. Jo, I. Jeong, J. Lee, *Nanoscale* **2013**, *5*, 4584.

[61] P.-Y. Chang, C.-H. Huang, R.-A. Doong, *Carbon* **2012**, *50*, 4259.

[62] J. Hwang, C. Jo, K. Hur, J. Lim, S. Kim, J. Lee, *J. Am. Chem. Soc.* **2014**, *136*, 16066.

[63] C. Jo, Y. Kim, J. Hwang, J. Shim, J. Chun, J. Lee, *Chem. Mater.* **2014**, *26*, 3508.

[64] Q. Lu, J. G. Chen, J. Q. Xiao, *Angew. Chem., Int. Ed.* **2013**, *52*, 1882.

[65] J. Jin, S.-Z. Huang, J. Liu, Y. Li, D.-S. Chen, H.-E. Wang, Y. Yu, L.-H. Chen, B.-L. Su, *J. Mater. Chem. A* **2014**, *2*, 9699.

[66] I. E. Rauda, L. C. Saldarriaga-lopez, B. A. Helms, L. T. Schelhas, D. Membreno, D. J. Milliron, S. H. Tolbert, *Adv. Mater.* **2013**, *25*, 1315.

[67] M. Epifani, P. Imperatori, L. Mirenghi, M. Schioppa, P. Siciliano, *Chem. Mater.* **2004**, *16*, 5495.

[68] P. Yang, D. Margolese, B. Chmelka, G. Stucky, *Nature* **1998**, *396*, 152.

[69] C. J. Brinker, Y. Lu, A. Sellinger, H. Fan, *Adv. Mater.* **1999**, *11*, 579.

[70] Q. Huo, D. Margolese, U. Ciesla, P. Feng, I. T. E. Gier, P. Sieger, R. Leon, P. Petroff, F. Schüth, G. D. Stucky, *Nature* **1994**, *368*, 317.

[71] C. T. Kresge, M. E. Leonowicz, W. J. Roth, J. C. Vartuli, J. S. Beck, *Nature* **1992**, *359*, 710.

[72] D. M. Antonelli, J. Y. Ying, *Chem. Mater.* **1996**, *8*, 874.

[73] Q. Huo, D. I. Margolese, U. Ciesla, D. G. Demuth, P. Feng, T. E. Gier, P. Sieger, A. Firouzi, B. F. Chmelka, F. Schuth, G. D. Stuckey, *Chem. Mater.* **1994**, *6*, 1176.

[74] H. Shi, *Electrochim. Acta* **1996**, *41*,1633.

[75] A. B. Fuertes, F. Pico, J. M. Rojo, *J. Power Sources* **2004**, *133*, 329.

[76] C. Largeot, C. Portet, J. Chmiola, P. Taberna, Y. Gogotsi, P. Simon, *J. Am. Chem. Soc.* **2008**, *130*, 2730.

[77] D. Qu, H. Shi, *J. Power Sources* **1998**, *74*, 99.

[78] A. B. Fuertes, G. Lota, T. A. Centeno, E. Frackowiak, *Electrochim. Acta* **2005**, *50*, 2799.

[79] P. J. Mulhern, *Can. J. Phys.* **1989**, *67*, 1049.

[80] F. Wypych, R. Schollhorn, *J. Chem. Soc., Chem. Commun.* **1992**, 1386.

[81] M. A. Py, R. R. Haering, *Can. J. Phys.* **1983**, *61*, 76.

[82] N. Imanishi, M. Toyoda, Y. Takeda, O. Yamamoto, *Solid State Ionics* **1992**, *58*, 333.

[83] L. F. Mattheiss, *Phys. Rev. B* **1973**, *8*, 3719.

[84] G. Eda, H. Yamaguchi, D. Voiry, T. Fujita, M. Chen, M. Chhowalla, *Nano Lett.* **2011**, *11*, 5111.

[85] H. Wang, Z. Lu, S. Xu, D. Kong, J. J. Cha, G. Zheng, P.-C. Hsu, K. Yan, D. Bradshaw, F. B. Prinz, Y. Cui, *Proc. Natl. Acad. Sci. USA* **2013**, *110*, 19701.

[86] C. A. Papageorgopoulos, W. Jaegermann, *Surf. Sci.* **1995**, *338*, 83.

[87] D. Yang, S. J. Sandoval, W. M. R. Divigalpitiya, J. C. Irwin, R. F. Frindt, *Phys. Rev. B* **1991**, *43*, 12053.

[88] V. Augustyn, P. Simon, B. Dunn, *Energy Environ. Sci.* **2014**, *7*, 1597.

[89] C. Zhong, Y. Deng, W. Hu, J. Qiao, L. Zhang, J. Zhang, *Chem. Soc. Rev.* **2015**, *44*, 7484.

[90] S. Ardizzone, G. Fregonara, S. Trasatti, *Electrochem. Acta* **1990**, *35*, 263.

[91] K.-M. Lin, K.-H. Chang, C.-C. Hu, Y.-Y. Li, *Electrochim. Acta* **2009**, *54*, 4574.

[92] C. Jo, I. Hwang, J. Lee, C. W. Lee, S. Yoon, *J. Phys. Chem. C* **2011**, *115*, 11880.

[93] S. W. Kim, D. H. Seo, X. Ma, G. Ceder, K. Kang, *Adv. Energy Mater.* **2012**, *2*, 710.

[94] V. Palomares, P. Serras, I. Villaluenga, K. B. Hueso, J. Carretero-González, T. Rojo, *Energy Environ. Sci.* **2012**, *5*, 5884.

[95] X. Wang, X. Shen, Z. Wang, R. Yu, L. Chen, *ACS Nano* **2014**, *8*, 11394.

FULL PAPER